Real space imaging of transient carrier dynamics by nanoscale pump-probe microscopy

Yasuhiko Terada, Shoji Yoshida, Osamu Takeuchi, and Hidemi Shigekawa*

Institute of Applied Physics, CREST-JST, University of Tsukuba, Tsukuba 307-8573 Japan

*http://dora.bk.tsukuba.ac.jp/

Smaller and faster are the key concepts in the progress of current nanoscience and technology. Thus, a method of exploring the transient carrier dynamics in organized nanostructures with pinpoint accuracy is eagerly desired. Real space imaging of nanoscale transient carrier dynamics with a wide range of lifetimes has been realized by pulse-laser-combined scanning tunneling microscopy (STM) with a noble delay time modulation method developed by a pulse-picking technique. A nonequilibrium carrier distribution is generated with ultrashort laser pulses and its relaxation processes are observed by STM on the basis of a pump-probe technique. The dynamics of the excited carriers modulated by the gap states associated with Co nanoparticle/GaAs has been directly analyzed and imaged in real space for the first time.

Understanding and control of the quantum dynamics, such as carrier transition and transport in nanoscale structures, are the key factors for continuing the advancement of nanoscale science and technology. However, with the miniaturization of functional devices consisting of composite materials, carrier dynamics, which has been analyzed by techniques providing spatially and/or temporally averaged information, does not provide a sufficient description for the analysis and designing of macroscopic functions. For example, atomic-scale defects have significantly changed the entire approach: defects, which were once considered as a problem to be avoided, are actively designed and controlled to realize desired functions [1]. The fluctuation in the distribution of dopant materials in the nanostructural components governs the characteristic properties of macroscopic functions of the total system. Therefore, the evaluation of the transient carrier dynamics in nanoscale potential landscapes of composite materials over a wide range of time scales is of great importance.

Currently, the development of ultrashort-pulse laser technology enables us to observe ultrafast dynamics in the femtosecond range. A prominent method is optical pump probe reflectivity (OPPR) measurement [2, 3]. Its spatial resolution, however, is generally limited by wavelength, and information is inevitably averaged over the nanoscale components, despite that they are organized with the greatest care to produce desired functions. In contrast, the real space observation of atomic-scale structures by scanning tunneling microscopy (STM) has lifted the veil from various longstanding problems and is extending the frontiers of science and technology [4-9]. However, since the temporal resolution of STM is limited to less than 100 kHz because of the circuit bandwidth, the target carrier dynamics has been beyond its field of vision. It has been one of the most challenging goals to combine STM with ultrashort-pulse laser

technology since the invention of STM.

Hamers et al. determined the recombination lifetime of photoexcited carriers in Si, in their pioneering work, by analyzing the observed surface photovoltage (SPV) by simulation [10], and a method that involves the combined use of an optical pulse pair and STM was proposed as photoconductive-gate STM (PG-STM) [11-18]. However, the spatial and temporal resolutions of the former method were limited to the 1 μm scale and laser-pulse repetition rate, respectively, and the PG-STM probes dI/dV or the quantity mediating the signal rather than the transient effect itself [18]. With the shaken-pulse-pair-excited STM (SPPX-STM) [19, 20], which was designed to detect a weak tunneling current of the transient signal under optical excitation, the time-resolved tunneling current in the subpicosecond range was successfully probed; however, its temporal range was very narrow and it was still difficult to reliably measure a very weak time-resolved STM signal in a short period of time, preventing the microscopy technique from revealing transient carrier dynamics in nanostructures consisting of composite materials with a wide variety of lifetimes. The long measurement time interferes the imaging of dynamics.

Here, we demonstrate a new methodology, which simultaneously realizes STM spatial resolution and the temporal resolution of the optical pump-probe technique, enabling the visualization of transient carrier dynamics in nanometer-scale structures with a wide variety of lifetimes. As an example, the first direct analysis of the hole capture rate via a gap state in a Co nanoparticle/GaAs structure is shown. The pinpoint probing and real space imaging of the carrier dynamics modulated by nanometer-scale structures have been realized.

Figure 1 shows a schematic of the microscopy technique that we developed and its

basic mechanism for probing. The surface of a sample beneath the STM tip is illuminated with a sequence of paired laser pulses with a certain delay time t_d, and the tunneling current I is measured as a function of t_d (Fig. 1**a**). In principle, we can obtain the temporal resolution of OPPR together with the spatial resolution of STM (see Mechanism in supplementary information).

To realize the desired microscopy, we developed the method of discrete and large modulation of delay time by using a pulse-picking technique (Fig. 1**b**, see Method), which, for the first time, has allowed the visualization of transient carrier dynamics in the nanometer-scale structures over a wide range of time scales. With the digital modulation of t_d between $t_d^{\,1}$ and $t_d^{\,2}$, the in-phase component obtained by the lock-in detection of the tunneling current gives $\Delta I(t_d^{\,1},t_d^{\,2}) \equiv I(t_d^{\,1}) - I(t_d^{\,2})$. As $t_d^{\,2}$ is set to a value larger than the relaxation time of the probed dynamics, $\Delta I(t_d^{\,1},t_d^{\,2})$ can be approximated as $\Delta I(t_d^{\,1}) \equiv I(t_d^{\,1}) - I(\infty)$, where $I(\infty)$ is the tunneling current for a delay time that is sufficiently long for the excited state to be relaxed. Since a large delay time to satisfy this condition, $t_d^{\,2} = \infty$, can be realized with the new microscopic technique, $\Delta I(t_d^{\,1})$ is accurately obtained through the lock-in detection of I by sweeping $t_d^{\,1}$. In addition, since the modulation can be performed at a high frequency (1 kHz in our case), the measurement is less affected by the low-frequency fluctuations in laser intensity and tunneling current. Accordingly, this method reduces the measurement time (1/10000 for our system) and hence enables the spatial mapping of time-resolved signals that has been desired for a long time.

Figure 2 shows the sample spectra obtained by this microscopic technique. For the

first time, the measurement of carrier dynamics over a wide range of time scales using one microscope has been achieved. The low-temperature-grown GaAs (LT-GaAs) region formed on a GaAs substrate exhibits an ultrafast decay component τ_b with a time constant of 2.4 ps, while the GaAs substrate region exhibits a time constant of 4.8 ns. These values are consistent with the recombination lifetimes determined from OPPR measurements, namely, 1.5 ps and 3.3 ns for the LT-GaAs and GaAs samples, respectively. Such agreement has been confirmed for various semiconductors with a wide range of lifetimes (Fig. S1 in Supplementary Information). The time resolution of this microscopy is limited only by the optical pulse width, which is 140 fs in the present case ("time resolution" in Supplementary Information). With this microscopy technique, probing of transient carrier dynamics in nanostructures consisting of composite materials with a wide range of lifetimes has been realized (Fig. S3).

When the delay time is changed over a wider time scale range, $\Delta I(t_d)$ shows a slower component with a time constant of about 100 ns for both GaAs and LT-GaAs regions, as a typical spectrum obtained for GaAs is shown in Fig. 3**a**. In STM on a semiconductor, a nanoscale metal-insulator-semiconductor (MIS) junction is formed by the STM tip, tunneling gap, and sample. Thus, when a reverse bias voltage is applied to the junction, tip-induced band bending (TIBB) occurs in the surface region owing to the leakage of the electric field into the sample [9,18,21]. With optical illumination, the redistribution of photocarriers reduces the electric field and changes the surface potential, which is called SPV, and increases the effective bias voltage applied to the tunnel junction. Consequently, the illumination increases the raw tunneling current I^* (Fig. 1**c**). The excited state subsequently relaxes to the original state through two processes. One is the decay of the photocarriers on the bulk side (bulk-side decay) via

recombination, drift and diffusion. The other is the decay of the carriers trapped at the surface (surface-side decay) via recombination and thermionic emission. Because of the lack of counterpart carriers near the surface, the surface-side decay constant is larger than the bulk-side decay constant.

The bulk-side decay is probed through the mechanism of absorption bleaching, which is a typical mechanism observed in the OPPR measurement. When the carriers excited by the first optical pulse remain in the excited state, the absorption of the second optical pulse is suppressed. In such a case, the second current pulse induced in I^* decreases and depends on t_d, reflecting the decay of the excited carriers after the first-pulse excitation (Figs. 1**c**-(ii) and 1**c**-(iii)). On the other hand, the surface-side decay is probed through the mechanism related to the SPV. If the surface carriers remain when the second optical pulse arrives, the electric field in the surface region remains low. Therefore, the excited photocarriers are less efficiently trapped at the surface, leading to a decrease in the SPV caused by the second optical pulse and in the height of the second current pulse in I^*. Accordingly, $\Delta I(t_d)$ is a measure of the surface-side carrier density at the delay time t_d as well as the bulk-side carrier density.

The decay constants for both components are derived from the fitting of $\Delta I(t_d)$ by a double exponential function; the small time constant τ_b is attributed to the bulk-side decay (Fig. 2 and Fig. S1), and the large time constant τ_S, to the surface-side decay (Fig. 3**a**). Since the recombination at the surface is enhanced for a large set-point tunneling current I_t, τ_s decreases as I_t increases. In contrast, the bulk-side carrier decay is not affected by the magnitude of I_t. Therefore, τ_b is independent of I_t. These expectations were confirmed, as shown in Fig. 3**b**; τ_s decreases with I_t, while τ_b remains almost constant. The linear relationship between signal amplitude and set-point tunneling

current (Fig. 3**c**) indicates that the time-resolved signal does not originate, for example, from photoelectrons and displacement current but from tunneling current (see "Mechanism" in the supplementary information).

Ultrafast carrier dynamics, which has been obtained only by optical methods using ultrashort-laser techniques, can be imaged in real space by STM. With this microscopic technique, both the recombination process of excited carriers and carrier dynamics, such as the diffusion and drift of carriers governed by local potential landscapes, can be probed through τ_b, which will be discussed elsewhere. Furthermore, since surface-side decay is affected, for example, by surface states and the probe is tunnel current with atomic-scale sensitivity, τ_S provides information about the modulation of carrier dynamics by a local atomic-level defect.

In the two decay components appearing in $\Delta I(t_d)$, the faster one is considered to reflect the decay of the bulk-side carriers, which are probed on the basis of absorption bleaching. This is well supported by fact that τ_b is consistent with the decay time obtained by the OPPR measurement for various samples (Fig. S1). On the other hand, the slower decay component (τ_s) has a complex dependence on sample bias voltage and tunneling current, which is consistent with the characteristic of surface-side carrier decay. Next, we show the results obtained for a Co/GaAs system, which provides more specific support for our mechanism, and this is the first demonstration that a meaningful physical quantity can be directly derived from the analysis of τ_s on the nanoscale.

If a deep level (or gap state) exists in a band gap, minority carriers are captured at the deep level with a high probability and then rapidly recombine with majority carriers. The modulation of carrier dynamics due to gap states significantly affects the properties of a device, and therefore a new method that enables the direct analysis of

gap-state-related processes at the nanoscale is strongly desired. As an example, we demonstrate the direct analysis of the hole capture rate via a Co-derived gap state.

Figure 4**a** shows an STM image of Co nanoparticles on an n-type GaAs surface. Co particles grow in the Volmer-Weber mode [22] on GaAs, and their size is controllable. The nanoparticle is typically 2 nm in size (~400 atoms), which is sufficiently large to form a gap-state level [23 24]. The existence of the gap-state level was confirmed by the experimental results we obtained; the I-V curves measured under laser illumination show that no photocurrent flows at the GaAs site while a fairly high photocurrent flows at a Co site at a low bias voltage (Vs ~ 0.1 V).

Figures 4**b** and 4**c** show the $\Delta I(t_d)$ curves measured at positions corresponding to bare GaAs and Co, respectively. The peak ratio of the bulk-side decay component to the surface-side decay component varies with the excitation intensity; the bulk-side decay diminishes as the excitation intensity increases. Here, we adjusted the excitation intensity to observe only surface-side decay. As expected, the decay constant at Co, 80 ns, is shorter than that at the bare GaAs surface, 220 ns.

A depletion layer is formed beneath the tip because of TIBB (Fig. 1d) in addition to the band bending induced by the gap states in the present case. The existence of TIBB was confirmed by the fact that although a large tunneling current flows when the sample is illuminated, a negligibly small current was observed in the dark even at a bias voltage higher than the band gap energy. The holes (minority carriers) photogenerated in the depletion layer drift to the surface and are rapidly captured at the gap states. However, the electrons (majority carriers) are depleted near the surface, and therefore no counterpart carriers exist that recombine with the holes captured at the gap states. The carrier decay time is nevertheless measured to be much shorter at Co because the

electrons are provided from the STM tip to the Co state via tunneling.

This is confirmed by the dependence of carrier decay time at Co on tunneling current (Fig. 4**e**). The decay time markedly decreases as tunneling current increases. In addition, the decay time is almost constant (T_{cap} = 6.9 ns) above a threshold current I_c (140 pA). From the analysis below, the hole capture probability P_h was derived as $P_h = 1/T_{cap} = 1.5 \times 10^8$ [s^{-1}].

The hole capture rate J_h is written as $J_h = P_h N_h$, where P_h is the probability per second that a hole in the depletion layer is captured at a gap state and N_h is the number of holes trapped at the surface after photoexcitation. The injection rate of electrons to a gap state J_e is proportional to the tunneling current I_t: $J_e = I_t/e$. Assuming that the rate of carrier recombination at the gap state is high [25], the recombination rate is equal to the lower rate, J_h or J_e. Thus, the recombination rate is J_e-limited when I_t is low, while it is J_h-limited and independent of I_t when I_t is high. In the J_h-limited regime, J_h varies with N_h, and the time evolution of N_h is written as,

$$\frac{dN_h}{dt} = -J_h = -P_h N_h, \quad N_h = N_{h0} \exp(-P_h t).$$

Here, the hole decay rate is equal to P_h.

For $I_c < I_t$ (J_h-limited regime), the gap state is filled with tunneling electrons, and even if N_h is large immediately after the photoexcitation, $J_h < J_e$ and the recombination rate is P_h, independent of I_t. Accordingly, the hole capture rate P_h can be directly derived from the decay time in this regime.

For $I_t < I_c$, on the other hand, N_h is large and $J_h > J_e$ immediately after the photoexcitation, and N_h initially linearly decays with time (A in Fig. 4**f**). Afterward, when N_h becomes small and $J_h < J_e$, N_h starts to decay exponentially (B in Fig. 4**f**). Thus,

the time evolution of N_h is represented as a black line in Fig. 4**f**. Since the S/N ratio was not sufficient to distinguish the difference between linear and exponential decay, the fit to the data was carried out with a single exponential function. Therefore, the apparent decay time derived from the fitting should be smaller than P_h^{-1}, which was indeed observed as shown in Fig. 4**e**.

When $I_t = I_c$, J_e is equal to J_h at the excitation time, this relation gives the number of holes N_{h0} photogenerated in the depletion layer and trapped beneath the tip. From Fig. 4**e**, I_c = 120 pA (J_e = 7.5 x 10^8 s^{-1}) and N_{h0} is derived to be 5.0. This value is comparable to the number of charges N_0 estimated to exist between a sphere of radius R and an infinite plane placed at a distance of 1 nm from the sample; N_0 is 15.5 for R = 10 nm and 40.7 for R = 20 nm.

The mechanism described above is also confirmed by its dependence on the sample bias voltage V_s. For a high V_s, the tip Fermi level is higher than the conduction band minimum of the sample. Since the tunneling probability for an electron is higher when its energy is closer to the vacuum level, electrons directly tunnel to the conduction band (Fig. 4**d**). In this case, the accelerated recombination via the gap state is less probable. This expectation was experimentally confirmed. For V_s = 2.5 V (Fig. 4**g**), the surface-side decay constant was 232 ns, comparable to that for the bare GaAs (Fig. 4**b**).

Next we show the spatial distribution of the surface-side decay of carriers (Fig. 5), which is the first demonstration of the real-space visualization of nanoscale carrier dynamics. The decay time is short directly above a Co dot and markedly increases when the tip is placed at a sub-nanometer distance away from it. This feature is consistent with the fact that the recombination is largely accelerated only when the tunneling

electrons are injected from the STM tip to the gap states formed by the Co dot.

Furthermore, the result shown in Fig. 5 confirms that the hole capture rate for each Co nanoparticle is distinguishable when the nanoparticles are at leaset 1nm apart. Accordingly, we measured T_{cap} for Co nanoparticles with different sizes (Fig. 5**d**). As the Co base area (S) increases, the capture probability is expected to increase and thus T_{cap} decreases, which corresponds well to the obtained result shown in Fig. 5**d**.

The new microscopy method has enabled the measurement of the carrier capture rate at a surface state and visualization of nanoscale carrier dynamics in real space. The solid line in Fig. 5**d** is the fit to the data with the simplified function $T_{cap} \sim 1/S$ [26]. The discrepancy in the fitting is considered to be due to a use of simplified model. Although further analysis is required, it is of great significance that our new microscopic technique provides data that can be used to discuss the dynamics in nanosystems.

As the device size deceases, such nanoscale modifications of carrier dynamics strongly affects the macroscopic device properties, and hence, the urgent task is to understand and control the correlation between the structural fluctuation and carrier dynamics.

By combining advanced ultrashort-pulse laser technology with STM, we have developed a new microscopy technique that visualizes the carrier dynamics in nanostructures with a wide range of lifetimes. We have visualized a carrier recombination process as an example, but other dynamical processes, such as carrier drift and diffusion, can also be imaged, making SPPX-STM applicable to the analysis of various composite materials in future devices. SPPX-STM is also applicable to systems in which the response of the in tunneling current has a nonlinear dependence on optical intensity. Detailed analysis of the mechanism is necessary for each dynamic property.

Tip effect on measurement must be included in the analysis. With the use of selected-wavelength and circularly polarized illumination, quantum transitions including excited and/or spin states may be included in probing processes. The direct observation of such dynamics is expected to enable further advances in nanoscale science and technology.

Method

As shown in Fig. 1**b**, pulse trains were generated by two synchronized Ti:sapphire lasers (*Mira* and *Chameleon, Coherent Inc*.) at a repetition rate of 90 MHz with a pulse width of 140 fs. The delay time between the two pulse trains could be continuously varied from zero to the pulse interval (~11 ns) by the synchronizing circuit (*Synchrolock, Coherent Inc*.) with a time jitter of 600 fs. Each train was guided to a pulse picker, which consisted of an ultrafast Pockels cell (*product*, *vendor*) and polarizers and is controlled by a homemade timing generator. The pulse picker selectively transmitted one pulse out of typically every 90 pulses, resulting in a pulse train with a reduced repetition rate of f_p (typically 1 MHz), while reducing the intensity of other pulses by a factor of 300. When the lifetime to be measured is longer than 0.5 μ s (= f_p /2), f_p is set to be lower than 1 MHz for optimizing measurement in accordance with the lifetime. By changing the relative timing of picking the pulses, an additional longer delay time was generated, which could be varied in multiples of the original pulse interval (~11 ns). Combining the short delay time generated by the synchronizing circuit and the longer delay time generated by the pulse pickers, the total delay time could be adjusted continuously from zero to as large value as required. Note that the reduced repetition rate can be selected to be as low as needed, which reduces the average laser intensity. Then, the two pulse trains were arranged onto the same light axis and guided into the STM (*VT-STM, Omicron NanoTechnology GmbH*). The light spot, with a diameter of less than 10 μm and an average intensity of up to several milliwatts, was focused on a sample surface below the STM tip using two lenses placed outside the ultra-high vacuum chamber (base pressure <1x10^{-8} Pa). The light spot was precisely positioned to maximize the SPV effect appearing in the tunnel current. All experiments discussed in this manuscript were carried out at room temperature.

The delay time modulation was achieved by changing the pulse-pick timing periodically at a

frequency of ~1 kHz. Namely, in the anterior half of the period, the picking is carried out at almost the same timing for the pump and probe pulse trains, while, in the posterior half of the period, the picking is carried out at a different by 180 degree. As a result, the delay time is modulated in a rectangular form between a relatively small value t_d (1 ps ~ 1 μs) and a very large value (0.5 μs-several μs), by which the ultrafast phenomena completely reached the steady state. Synchronously with the delay time modulation, the tunnel current signal from the STM preamplifier with a bandwidth of ~10 kHz is phase-sensitively detected by a lock-in amplifier. By virtue of the rectangular modulation of the delay time, the output of the lock-in amplifier is proportional to the difference between the tunnel current at the two delay times. In particular, when the larger delay time is set to be sufficiently long for the transient phenomena to reach the steady state, the signal becomes proportional to $\Delta I = I(t_d) - I(\infty)$. This novel technique using pulse pickers to modulate the delay time in a rectangular form with a large amplitude and a high modulation frequency is essential for maximizing the S/N ratio to achieve nanometer spatial resolution simultaneously with sub-picosecond time resolution.

References

1. Shinada, T., Okamoto, S., Kobayashi, T., & Ohdomari, I. Enhancing semiconductor device performance using ordered dopant arrays *Nature* **437**, 1128-1131 (2005).
2. Shah, J. Ultrafast Spectroscopy of Semiconductors and Semiconductor Nanostructures (Springer, Berlin, 1999).
3. Othonos, A. Probing ultrafast carrier and phonon dynamics in semiconductors. *J. Appl. Phys.* **83**, 1789-1830 (1998).
4. Binning, G., Rohrer, H., Gerber, Ch. & Weibel, E. Surface studies by scanning tunneling microscopy. *Phys. Rev. Lett.* **49**, 57-61 (1982).
5. Crommie, M. F., Lutz, C. P. & Eigler, D. M. Confinement of Electrons to Quantum Corrals on a Metal Surface. *Science* **262**, 218-220 (1993).
6. Wiesendanger, R. (ed.) Scanning Probe Microscopy and Spectroscopy: Methods and Applications (Cambridge University Press, Cambridge, 1994).
7. Heinrich, A. J., Lutz, C. P., Gupta, J. A., Eigler, & D. M. Molecule cascades. *Science* **298**, 1381-1387 (2002).
8. Lee, J. et al. Bandgap modulation of carbon nanotubes by encapsulated metallofullerenes. Nature **415**, 1005-1008. (2002).
9. Yoshida, S. et al. Microscopic basis for the mechanism of carrier dynamics in an operating p-n junction examined by using light-modulated scanning tunneling spectroscopy. *Phys. Rev. Lett.* **98**, 026802 (2007).
10. Hamers, R. J. & Cahill, D. G. Ultrafast time resolution in scanned probe microscopies. *Appl. Phys. Lett.* **57**, 2021-2033 (1990).
11. Nunes Jr. G & Freeman M R Picosecond resolution in scanning tunneling

microscopy. *Science* **262**, 1029-1032 (1993).

12. Weiss, S., Ogletree, D. F., Botkin, D., Salmeron, M. & Chemla, D. S. Ultrafast scanning probe microscopy. *Appl. Phys. Lett.* **63**, 2567-2569 (1993).
13. Botkin, D., Glass, J., Chemla, D. S., Ogletree, D. F., Salmeron, M. & Weiss, S. Advances in ultrafast scanning tunneling microscopy. *Appl. Phys. Lett.* **69**, 1321-1323 (1996).
14. Groeneveld, R. H. M. & van Kempen, H. The capacitive origin of the picosecond electrical transients detected by a photoconductively gated scanning tunneling microscope. *Appl. Phys. Lett.* **69**, 2294-2296 (1996).
15. Pfeiffer, W. et al. Photoelectron emission in femtosecond laser assisted scanning tunneling microscopy. *Appl. Phys. B.* **64**, 265-268 (1997).
16. Keil, U. D., Jensen, J. R. & Hvam, J. M. Transient measurements with an ultrafast scanning tunneling microscope. *Appl. Phys. Lett.* **72**, 1644-1646 (1998).
17. Khusnatdinov, N. N., Nagle, T. J. & Nunes, Jr. G. Ultrafast scanning tunneling microscopy with 1nm resolution. *Appl. Phys. Lett.* **77**, 4434-4436 (2000).
18. Grafström, S. Photoassisted scanning tunneling microscopy. *J. Appl. Phys.* **91**, 1717-1753 (2002).
19. Takeuchi, O. et al. Probing subpicosecond dynamics using pulsed laser combined scanning tunneling microscopy. *Appl. Phys. Lett.* **85**, 3268-3270 (2004).
20. Terada, Y. et al. Ultrafast photoinduced carrier dynamics in GaNAs probed using femtosecond time-resolved scanning tunneling microscopy. *Nanotechnology* **18**, 044028 (2007).
21. Kronik, L. & Shapira, Y. Surface photovoltage phenomena: theory, experiment, and applications. *Surf. Sci. Rep.* **37**, 1-206 (1999).

22. Campbell, C. T. Ultrathin metal films and particles on oxide surfaces: structural, electronic and chemisorptive properties. *Surf. Sci. Rep.* **27**, 1-111 (1997).

23. Nilius, N., Wallis, T., & Ho, W. Development of one-dimensional band structure in artificial gold chains. *Science* 297, 1853 (2002).

24. Firt, P., Stroscio, J., Dragoset, R., Pierce, D., & Celotta, R. Metallicity and gap states in tenneling to Fe clusters on GaAs(100). *Phys. Rev. Lett.* **63**, 1416 (1989).

25. Sze, S. M. *Physics of Semiconductor Devices* (John Wiley, New York, 1981).

26. Schockley, W & Read, W. T. Jr. Statics of the Recombinations of Holes and Electrons. *Phys. Rev. Lett.* **87**, 835-842 (1952).

Figure captions

Figure 1 Schematic illustrations of the microscopy system and its probe mechanism. a-b, Optical pulses from the two synchronized Ti-sapphire oscillators are selectively transmitted using pulse pickers and coaxially aligned to produce a sequence of paired pulses with a certain delay time, t_d. Pulse pairs with a central wavelength of 800 nm and an average intensity of 1 mW were focused to less than 10 μm and tunnel current was measured. **c,** Relationship between raw tunneling current I^* and delay time t_d. **d,** Measured tunneling current I as a function of delay time, where delay times of (i), (ii) and (iii) correspond to those of (i), (ii) and (iii) in **c**.

Figure 2 Wide range of time scales measured using the developed microscopy. $\Delta I(t_d)$ vs t_d curves obtained for **a** LT-GaAs, **b** GaNAs, **c** undoped GaAs, and **d** hydrogen-terminated Si(111) (n-type, 0.5 Ωcm). The decay constants derived by fitting are **a** 2.4 ps, **b** 440 ps, **c** 4.8 ns, and **d** 0.87 μs. See "Fitting procedures" in Supplementary Information for more details.

Figure 3 Bulk-side and surface-side carrier decays reflected in $\Delta I(t_d)$. a, Typical spectrum obtained for GaAs over a wider time scale range (V_s = 5.5 V, I_t = 40 pA). The components with small and large time constants τ_b and τ_b represent the bulk-side and surface-side decays, respectively. **b** and **c,** Dependence of the decay constants on set-point tunneling current I_t (V_s = 5 V).

Figure 4 Carrier recombination via Co nanoparticle/GaAs gap states. a, STM

image of Co nanoparticles on a GaAs(110) surface. **b and c**, SPPX signals measured above bare GaAs and a Co particle. **d**, Schematic illustrations of surface-side recombination. **e**, Tunneling current dependence of carrier decay time at Co (V_s = 2 V). **f**, Two decay modes when $I_t < I_c$. **g**, SPPX-STM signal at a high bias voltage.

Figure 5 Real-space imaging of decay time. STM image **a** and 2D mapping of time-resolved signal **b** obtained for Co nanodot/GaAs(110) system. **c,** Superimposed display of **a** and **b**. **d,** Cross section along line in **b**. Showing size dependence of hole capture rate.

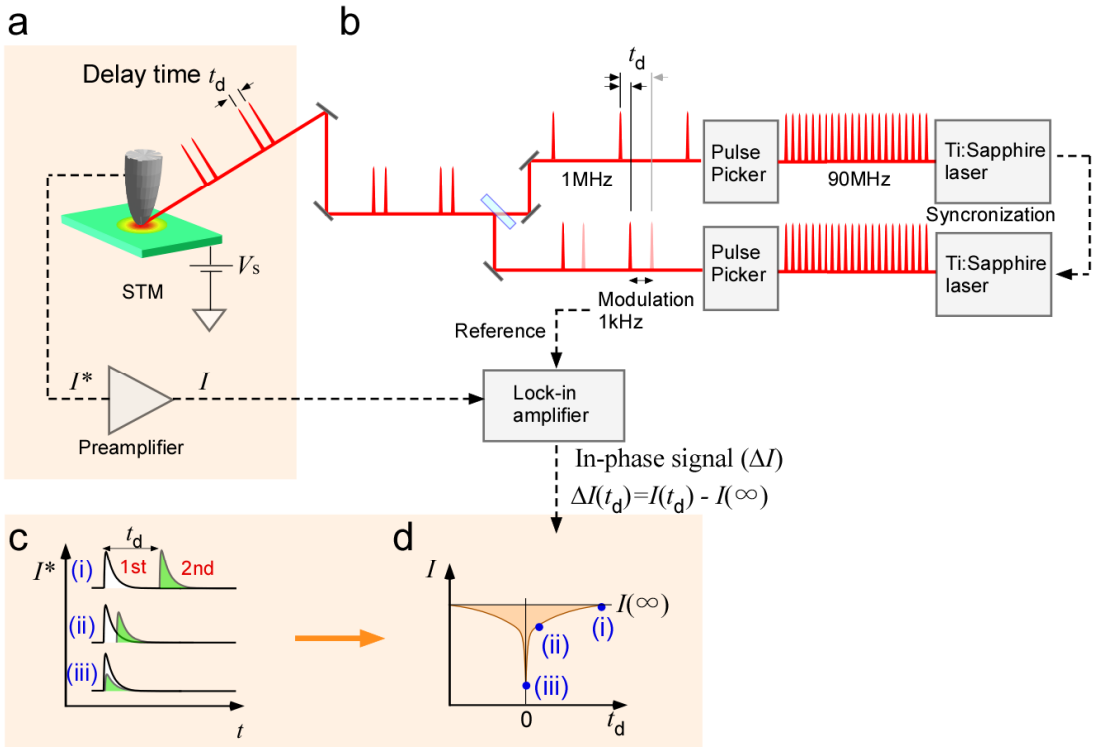
a
b
Delay time t_d
STM
V_S
I^*
I
Preamplifier
t_d
1MHz
Pulse Picker
90MHz
Ti:Sapphire laser
Syncronization
Pulse Picker
Ti:Sapphire laser
Modulation 1kHz
Reference
Lock-in amplifier
In-phase signal (ΔI)
$\Delta I(t_d)=I(t_d) - I(\infty)$
c
I^*
(i)
1st
2nd
(ii)
(iii)
t
d
I
$I(\infty)$
(i)
(ii)
(iii)
0
t_d

Fig. 1

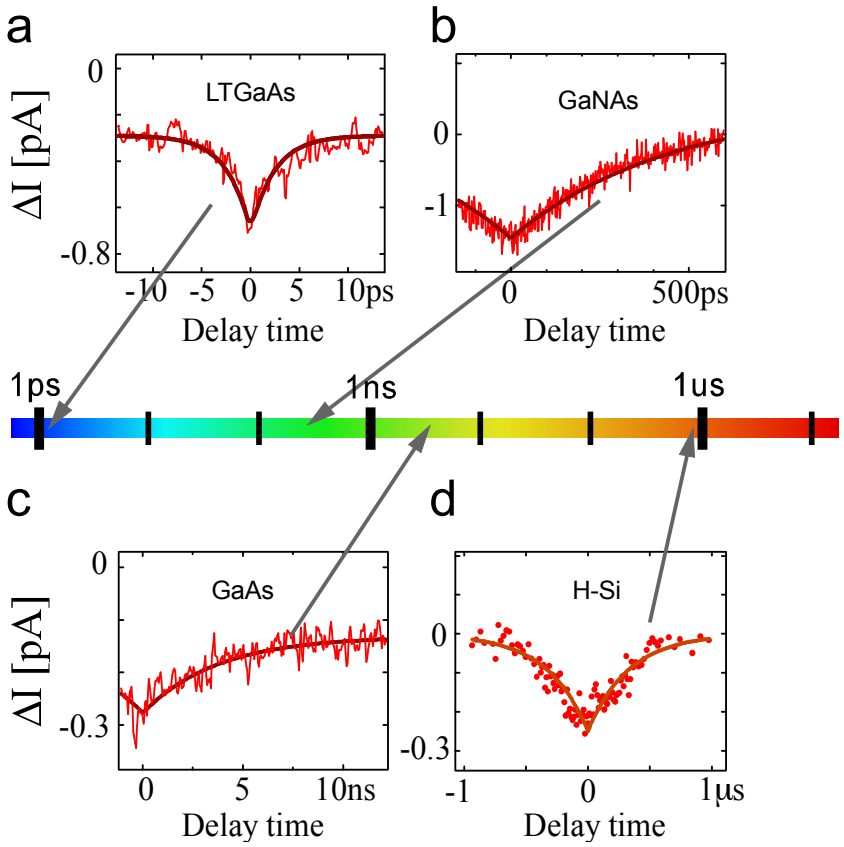
a
b
LTGaAs
GaNAs
ΔI [pA]
0
-0.8
-10 -5 0 5 10ps
Delay time
0
-1
0 500ps
Delay time
1ps
1ns
1us
c
d
GaAs
H-Si
0
-0.3
0 5 10ns
Delay time
-1 0 1μs
Delay time

Fig. 2

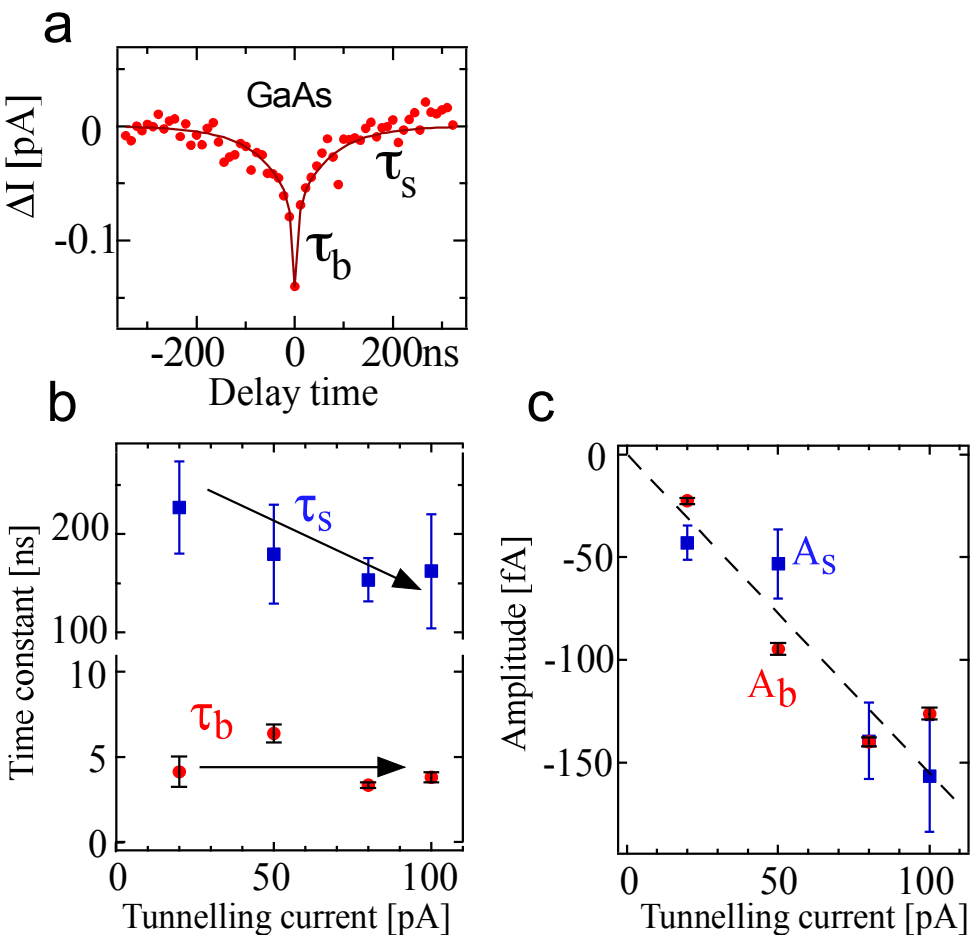
a
GaAs
ΔI [pA]
0
-0.1
τs
τb
-200
0
200ns
Delay time
b
Time constant [ns]
200
100
10
5
0
τs
τb
0
50
100
Tunnelling current [pA]
c
Amplitude [fA]
0
-50
-100
-150
As
Ab
0
50
100
Tunnelling current [pA]

Fig. 3

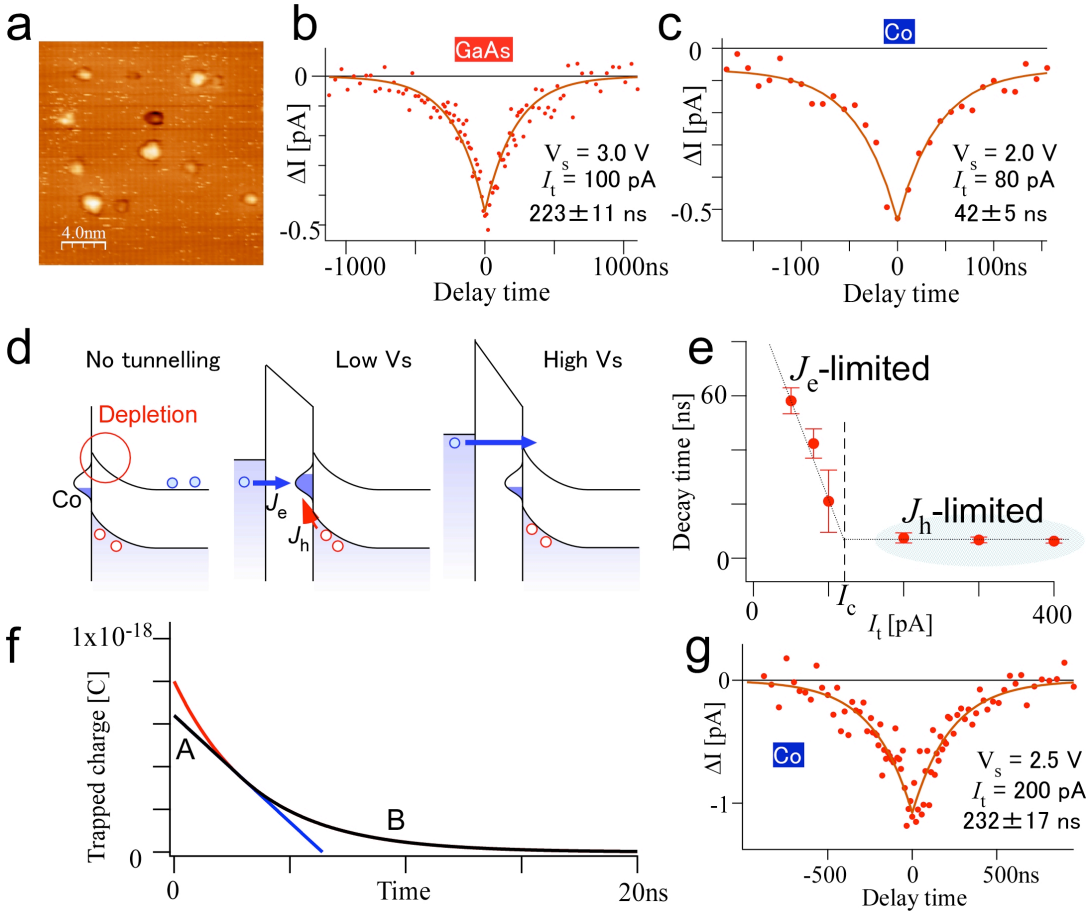
a
4.0nm
b
GaAs
0
-0.5
ΔI [pA]
V_s = 3.0 V
I_t = 100 pA
223±11 ns
-1000
0
1000ns
Delay time
c
Co
0
-0.5
ΔI [pA]
V_s = 2.0 V
I_t = 80 pA
42±5 ns
-100
0
100ns
Delay time
d
No tunnelling
Low Vs
High Vs
Depletion
Co
J_e
J_h
e
J_e-limited
J_h-limited
Decay time [ns]
60
0
0
I_c
I_t [pA]
400
f
1x10^{-18}
Trapped charge [C]
A
B
0
0
Time
20ns
g
0
-1
ΔI [pA]
Co
V_s = 2.5 V
I_t = 200 pA
232±17 ns
-500
0
500ns
Delay time

Fig. 4

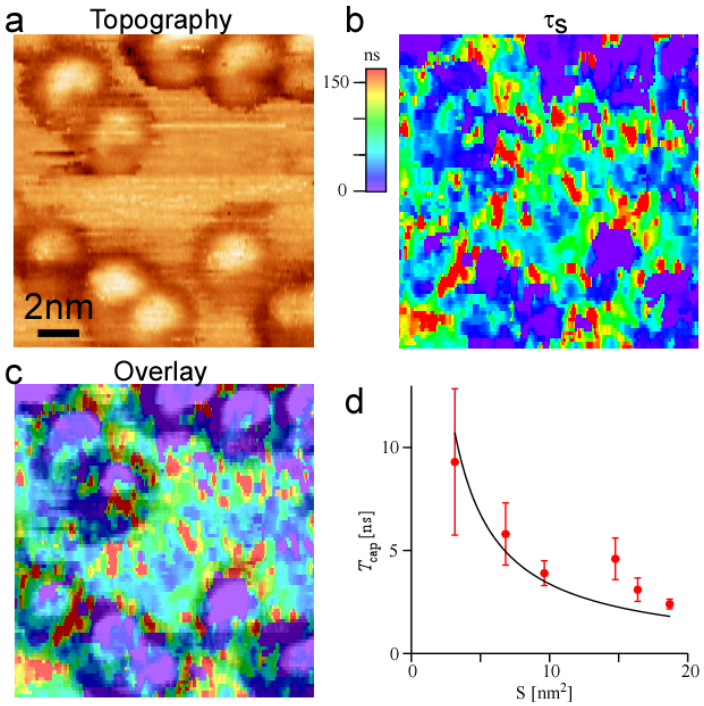
a
Topography
2nm
b
τs
ns
150
0
c
Overlay
d
10
5
0
T_{cap} [ns]
0
10
20
S [nm^2]

Fig. 5